Xu et al. *Zool. Res.* 2023, 44(1): 63−77
https://doi.org/10.24272/j.issn.2095-8137.2022.167

ZR | Zoological Research

Article Open Access

# Depletion of *stearoyl-CoA desaturase* (*scd*) leads to fatty liver disease and defective mating behavior in zebrafish

Shan-Shan Xu[1,2], Yi Li[2], Hou-Peng Wang[2], Wen-Bo Chen[1], Ya-Qing Wang[2], Zi-Wei Song[1], Hui Liu[1], Shan Zhong[1,4,*], Yong-Hua Sun[2,3,*]

[1] *Department of Genetics*, *Wuhan University School of Basic Medical Sciences*, *Wuhan*, *Hubei* 430071, *China*
[2] *State Key Laboratory of Freshwater Ecology and Biotechnology*, *Hubei Hongshan Laboratory*, *Institute of Hydrobiology*, *Innovation Academy for Seed Design (INASEED)*, *Chinese Academy of Sciences*, *Wuhan*, *Hubei* 430072, *China*
[3] *College of Advanced Agricultural Sciences*, *University of Chinese Academy of Sciences*, *Beijing* 100049, *China*
[4] *Hubei Province Key Laboratory of Allergy and Immunology*, *Wuhan*, *Hubei* 430071, *China*

**ABSTRACT**

Stearyl coenzyme A desaturase (SCD), also known as delta-9 desaturase, catalyzes the rate-limiting step in the formation of monounsaturated fatty acids. In mammals, depletion or inhibition of SCD activity generally leads to a decrease in triglycerides and cholesteryl esters. However, the endogenous role of *scd* in teleost fish remains unknown. Here, we generated a zebrafish *scd* mutant (*scd*$^{-/-}$) to elucidate the role of *scd* in lipid metabolism and sexual development. Gas chromatography-mass spectrometry (GC-MS) showed that the *scd*$^{-/-}$ mutants had increased levels of saturated fatty acids C16:0 and C18:0, and decreased levels of monounsaturated fatty acids C16:1 and C18:1. The mutant fish displayed a short stature and an enlarged abdomen during development. Unlike *Scd*$^{-/-}$ mammals, the *scd*$^{-/-}$ zebrafish showed significantly increased fat accumulation in the whole body, especially in the liver, leading to hepatic mitochondrial dysfunction and severe cell apoptosis. Mechanistically, *srebf1*, a gene encoding a transcriptional activator related to adipogenesis, *acc1* and *acaca*, genes involved in fatty acid synthesis, and *dgat2*, a key gene involved in triglyceride synthesis, were significantly upregulated in mutant livers to activate fatty acid biosynthesis and adipogenesis. The *scd*$^{-/-}$ males exhibited defective natural mating behavior due to defective genital papillae but possessed functional mature sperm. All defects in the *scd*$^{-/-}$ mutants could be rescued by ubiquitous transgenic overexpression of *scd*. In conclusion, our study demonstrates that *scd* is indispensable for maintaining lipid homeostasis and development of secondary sexual characteristics in zebrafish.

**Keywords:** Zebrafish; *scd*; Liver; Lipid homeostasis; Reproduction

Received: 11 August 2022; Accepted: 26 October 2022; Online: 26 October 2022

Foundation items: This study was supported by the Strategic Priority Research Program of the Chinese Academy of Sciences (XDA24010108), National Natural Science Foundation of China (31872554, 32172952), and Project from the State Key Laboratory of Freshwater Ecology and Biotechnology (2019FBZ05)

*Corresponding authors, E-mail: zhongshan@whu.edu.cn; yhsun@ihb.ac.cn

## INTRODUCTION

*De novo* lipogenesis, the synthesis of fatty acids and triglycerides from glucose, produces saturated fatty acids, such as palmitate (16:0) (Jump, 2011). Stearyl coenzyme A desaturase (SCD), also known as delta-9 desaturase, is a rate-limiting enzyme in the synthesis of monounsaturated fatty acids, mainly oleate (18:1) and palmitoleate (16:1), which are key substrates for triacylglyceride (TAG) generation and lipid storage (Hulver et al, 2005).

The function of the *SCD* genes has been extensively studied using mammalian models. So far, four *SCD* genes have been identified in mice (Miyazaki et al, 2003; Ntambi et al, 1988; Tabor et al, 1998; Zheng et al, 2001). Among them, *Scd1* and *Scd2* are mainly expressed in adipogenic tissues, such as the liver and adipose tissue, while *Scd3* is mainly expressed in the skin, epithelial glands, and Harder's glands, and *Scd4* is mainly expressed in the heart (Miyazaki et al, 2003; Ntambi & Miyazaki, 2003; Zheng et al, 2001). SCD1 plays an important role in lipid metabolism and body weight regulation in mice (Dobrzyn et al, 2015; Sampath & Ntambi, 2014). *Scd1* mutant mice show increased energy expenditure, reduced body fat accumulation, and increased skeletal muscle sensitivity to insulin (Dobrzyn et al, 2004; Malodobra-Mazur et al, 2014; Miyazaki et al, 2007; Ntambi et al, 2002). In *Scd1*-deficient mice, adenosine monophosphate (AMP)-activated protein kinase (AMPK) phosphorylation and activity are significantly increased, resulting in the down-regulation of genes involved in fatty acid synthesis and up-regulation of genes involved in fatty acid oxidation and β-oxidation (Dobrzyn et al, 2005; Dobrzyn et al, 2004; Kim et al, 2011). SCD1 also plays a role in regulating lipid mobilization of adipocytes by changing the composition of fatty acids (Zou et al, 2020), with overexpression of SCD1 found to induce lipolysis via the up-regulation of lipase and fat phagocytic pathways, further promoting fat mobilization and energy expenditure.

Under the challenges of population growth and food security, fish are an important source of high-quality protein for humans. Instead of using carbohydrates efficiently, fish use protein for energy, thus limiting their dietary protein stores. Protein deposition depends on protein turnover balance, which is closely related to cellular energy homeostasis. Mitochondrial fatty acid β-oxidation (FAO) plays a crucial role in energy metabolism. Inhibition of mitochondrial FAO in fish induces energy homeostasis remodeling and enhances glucose utilization and protein deposition (Li et al, 2020). Therefore, farmed fish with suppressed mitochondrial FAO may exhibit high potential to utilize carbohydrates to increase protein deposition by modulating energy homeostasis (Li et al, 2020). Nutritional manipulation of laying hen diets to include sources of n-3 fatty acids promotes the deposition of these nutrients into egg yolk, with n-3 fatty acid-rich eggs potentially providing an alternative food source to enhance consumer intake of these proposed healthful fatty acids (Van Elswyk, 1997). Previous research has indicated that a lack of △5 desaturase activity impairs eicosapentaenoic acid (EPA) and docosahexaenoic acid (DHA) synthesis in Red Sea bream and Japanese flounder cells (Nyunoya et al, 2021). Transgenic zebrafish and common carp enriched in n-3 fatty acids are protected from abnormal lipid deposition in the liver (Pang et al., 2014; Sun et al., 2020a; Zhang et al, 2019). Zebrafish are considered an important model for studying lipogenesis and fatty liver disease (Hölttä-Vuori et al, 2010; Quinlivan & Farber, 2017). Lipid metabolism is also tightly linked to reproduction and reproductive health (Hansen et al, 2013). Therefore, lipid metabolism in fish is an important topic in both aquaculture and biomedical research. In zebrafish genome, there are two *Scd* homologues, *scd* and *scdb*. However, whether and how *scd* regulates lipid homeostasis and reproduction in teleosts remains unclear.

In the present study, we generated zebrafish *scd* mutants *($scd^{-/-}$)* using CRISPR/Cas9 to elucidate the role of *scd* in lipid metabolism and reproductive development. Adult zebrafish lacking *scd* were characterized by a short body length and severe fat accumulation and apoptosis in the liver, which could be rescued by overexpression of *scd*. Mutant males displayed abnormal mating behavior due to defective secondary sexual characteristics. Our study shows that s*cd* is indispensable for maintaining lipid metabolism and reproductive development in zebrafish.

## MATERIALS AND METHODS

### Zebrafish

Wild-type (WT) AB strain zebrafish (China Zebrafish Resource Center, National Aquatic Biological Resource Center, CZRC/NABRC, Wuhan, China; http://zfish.cn) were obtained and maintained at the proper density. All experiments involving the zebrafish were performed under the approval of the Institutional Animal Care and Use Committee of the Institute of Hydrobiology, Chinese Academy of Sciences (protocol IHB2016-002).

### Generation of *scd* and *scdb* mutants

Gene knockout was performed using CRISPR/Cas9 technology, as described previously (Sun et al, 2020b). Briefly, the target sequences of *scd* (CCGTCTGCACACCCGCTCAC) and *scdb* (GTGCTCTAGGAATAACTGCCGG) are located in the second exon. Guide RNA (gRNA) was synthesized using a Transcript Aid T7 High-Yield Transcription Kit (K0441, Thermo Fisher Scientific, USA) and Cas9 mRNA was synthesized using a T3 mMESSAGE mMACHINE mRNA Transcription Synthesis Kit (AM1344, Thermo Fisher Scientific, USA) following the manufacturers' instructions. Single-cell embryos were co-injected with 2 nL of solution containing 400 ng/μL Cas9 mRNA and 50 ng/μL gRNA. To confirm mutation, genomic DNA was extracted from the tail fin and polymerase chain reaction (PCR) was performed to amplify the genomic DNA containing the target site, followed by sequencing of the PCR product to identify the mutation type.

### Whole-mount *in situ* hybridization of embryos

PCR-amplified sequences of genes of interest were used as templates for the synthesis of an antisense RNA probe, labeled with digoxigenin-linked nucleotides. Whole-mount *in situ* hybridization of embryos was performed as described previously (Thisse et al., 2008).

### *In situ* hybridization of gonadal sections

*In situ* hybridization was performed on frozen sections as described previously (Wang et al, 2022). Briefly, 10 μm-thick slices were made on a freezing microtome (Leica, Germany), then fixed in 4% paraformaldehyde (PFA) for 15 min at room temperature and washed three times in phosphate-buffered saline (PBS) 5 min each time. The slices were incubated with the probe at 70 °C overnight, then incubated with secondary antibodies at room temperature (23 °C) for 3 h. Images were acquired using a microscope (Zeiss AXIO Scope A1, Germany) equipped with a Spot digital camera.

### Measurement of body weight, body length, and sex ratio

The WT, heterozygous *scd* mutant *(scd*$^{+/-}$*)*, and *scd*$^{-/-}$ mutant fish derived from crosses of *scd*$^{+/-}$ fish were raised in the same aquarium until they reached a certain age, then used for genotyping. The rearing density of fish was 50 larvae/L from 5 days post-fertilization (dpf) to 15 dpf, 20 fish/L from 15 dpf to 1 month post-fertilization (mpf), 10 fish/L from 1 mpf to 2 mpf, and 5 fish/L from 2 mpf and older. After anesthetization, body weight and body length of WT and *scd*$^{-/-}$ fish were measured individually. Sexes of WT, *scd*$^{+/-}$, and *scd*$^{-/-}$ fish at 6 mpf were determined according to secondary sexual characteristics.

### *In vitro* fertilization assay

Both WT and *scd*$^{-/-}$ zebrafish (6 mpf) were used for *in vitro* fertilization analysis. First, the genital pores were wiped dry, and semen was aspirated using a pipette tip under a microscope. The female abdomen was gently pressed to express the eggs. Semen was then added to the eggs for insemination, followed by the addition of water. After 5 min, the fertilized embryos were transferred to a large dish for 3 h and counted under a stereo microscope.

### Mating behavior assay

Mating behavior was evaluated by recording videos of the process in the spawning tank as described in (Zhang et al, 2020). Recording started 10 min after the partition was removed in the breeding tank and lasted for 10 min (each group). The ZebraBox system (ViewPoint Life Sciences, Canada) was used to analyze mating behavior. Contact between two fish was defined as a distance of less than 1 cm. Contact frequency was defined as the number of contacts every 5 s. Contact frequency data were analyzed and graphed using GraphPad Prism v7.0.

### RNA extraction and quantitative real-time PCR (RT-qPCR)

Adult WT zebrafish were dissected to obtain different tissues. Total RNA in each tissue was extracted using TRIZOL (Invitrogen, America) according to conventional methods. RNA (1 μg) was used for reverse transcription (Takara Reverse Transcription Kit, Japan) to synthesize cDNA, and 1 μL of cDNA was used for each reaction. PCR amplification was performed using iTaq$^{TM}$ Universal SYBR Green Supermix on a CFX Connect Real-Time System (BioRad, USA). RT-qPCR was performed according to the MIQE (Minimum Information for Publication of Quantitative Real-Time PCR Experiments) guidelines (Bustin et al, 2009). *β-actin* was used as a reference gene for RT-qPCR as its expression was unchanged in the WT and mutant livers. All data were analyzed as described previously (Livak & Schmittgen, 2001).

### Immunofluorescence staining of tissue sections

Testicular tissue sections were used for immunofluorescence assays. After washing with 1×PBS to remove PFA, the sections were permeabilized with 0.5% Triton X-100 (Sigma-Aldrich, America) in PBS at room temperature for 15 min, washed three times in 1×PBS containing 1% bovine serum albumin (BSA), 0.1% Triton-100, and 1% dimethyl sulfoxide (DMSO), then blocked for 1 h. The sections were then incubated with primary antibodies (1:1 000 rabbit anti-Vasa and 1:1 000 rabbit anti-PCNA, Cell Signaling Technology, 3377S; and 1:200 rabbit anti-Sycp3, ab150292) in blocking solution overnight at 4 °C, and then with secondary antibodies (1:1 000, anti-rabbit IgG, Alexa Fluor 488) overnight at 4 °C in the dark. The sections were counterstained with 1 μg/mL 4',6-diamidino-2-phenylindole (DAPI) for 20 min at room temperature, then counterstained with 75% glycerol containing anti-fading agent. In addition, 3 mpf testes were stained with phalloidin-Alexa Fluor 568 (Molecular Probes). The samples were imaged under a SP8 confocal microscope (Leica, Germany), then processed using ImageJ (v1.8.0).

### Cell apoptosis detection

The zebrafish were anesthetized, and livers were dissected. Frozen tissue sections were prepared and incubated with 4% PFA for 30 min at room temperature. Subsequently, TUNEL staining was performed to evaluate liver apoptosis using a TUNEL Apoptosis Detection Kit (Yeasen, Cat. 40306ES50, China). In the liver tissue sections, DAPI was used for nuclear staining and TUNEL staining was used to indicate apoptosis signals. In each experiment, three fluorescence micrographs were taken using a Leica SP8 confocal microscope (Leica, Germany), and images were processed with ImageJ (v1.8.0).

### Transmission electron microscopy

After sampling, the WT and *scd*$^{-/-}$ livers were fixed in electron microscopy fixative (glutaraldehyde) for 30 min. Electron microscopy and transmission electron microscopy of the fixed tissues were performed by Wuhan Saiweier Biotechnology Co., Ltd. (China).

### RNA purification and sequencing

Total RNA was extracted using an RNA Extraction Kit (Nanjing Novizan Biotechnology Company, China). A NanoDrop 2000c spectrometer (Thermo Scientific, USA) was used to measure RNA concentration, and 1% agarose gel electrophoresis was used to measure RNA sample purity. RNA quality was confirmed by A260/A280. DNase I was used to eliminate DNA. Libraries for RNA sequencing (RNA-seq) were constructed using a SMARTer PCR cDNA Synthesis Kit (Takara, Japan). Finally, libraries were sequenced and 150 bp paired end reads were produced using the Illumina NovaSeq platform as described previously (Ye et al., 2022).

### Read mapping and expression level estimation

Low-quality reads containing >5% N or >20% bases with quality <Q20 (percentage of sequences with sequencing error rates <1%) and adaptor sequences were removed using TrimGalore v0.6.6. Clean data were aligned to the *Danio rerio* reference genome (z11) by STAR v2.7.1a using default

parameters. FeatureCounts v1.5.2 was used to quantify the expression level of each gene (parameters: -t exon, -g gene name). Transcripts per kilobase of exon model per million mapped reads (TPM) were calculated for each gene.

**Differential expression analysis**

Differentially expressed genes (DEGs) between sample groups were assessed using DESeq2. The false discovery rate (FDR) was used to identify the *P*-value threshold in multiple tests to determine significance of differences. Here, genes with Fold-Change>2 and adjusted *P*-value<0.05 were considered as DEGs.

**Pathway enrichment analysis**

The R package clusterProfiler v3.16.1 was used for functional enrichment analysis of Gene Ontology (GO) biological processes and Kyoto Encyclopedia of Genes and Genomes (KEGG) pathways. *P*-values were corrected based on the Benjamini and Hochberg (BH) method and adjusted *P*-value<0.05 was considered statistically significant.

**Statistical analysis**

Results are expressed as mean±standard error of the mean (*SEM*). For analysis of RT-qPCR, expression area, body weight, body length, natural mating success rate, contact frequency, fertilization rate, and TUNEL assay, we used unpaired *t*-tests (*P*<0.05, *P*<0.01, or *P*<0.001). For analysis of sex ratio in WT, $scd^{+/-}$, and $scd^{-/-}$ fish, we used two-way analysis of variance (ANOVA), followed by Sidak's multiple comparisons test (*P*<0.05). GraphPad Prism v7.0 was used for all statistical analyses.

## RESULTS

**Generation, identification, and characterization of zebrafish *scd* mutants**

The two SCD homologues in the zebrafish genome, i.e., *scd* and *scdb*, were located on chromosomes 12 and 13, respectively (Supplementary Figure S1). Gene syntenic analysis suggested that zebrafish *scd*, not *scdb*, was the orthologue of human *SCD* and mouse *Scd1*. Zebrafish Scd contained a specific domain of the fatty acid desaturase superfamily. The sequence homology of SCD in different fish species ranged from 76.42% to 80.36% (Supplementary Figure S2A, C), and in different vertebrate species ranged from 56.62% to 84.12% (Supplementary Figure S2B, D). Transmembrane domain analysis of the zebrafish SCD protein sequences identified four transmembrane domains. Sequence alignment analysis suggest that SCD is highly conserved in structure and function during evolution. Embryo *in situ* hybridization showed that *scd* was expressed in all embryonic stages in zebrafish, while *scdb* was only expressed in the early stage (Figure 1A, B). RT-qPCR was used to analyze the expression profiles of *scd* in different stages of development in WT zebrafish. Results showed that *scd* expression was higher in 1 hour post-fertilization (hpf) and 120 hpf embryos (Figure 1C). Between 1 hpf and 120 hpf, *scd* expression initially decreased and then increased. Similarly, we analyzed the expression profiles of *scd* in different tissues in WT zebrafish and found that *scd* was expressed in different tissues (Figure 1D), with relatively high expression levels in the liver, brain, and ovary (Figure 1D).

To investigate the *in vivo* function of *scd* in zebrafish, we generated *scd* knockout zebrafish on a WT background using CRISPR/Cas9. We targeted exon 2 to disrupt the translation of all functional domains (Figure 1E). We used genetic screening and sequencing to confirm the mutations and identified two homozygous mutant alleles of *scd*. The mutation occurred in the catalytic region of desaturase, and the frame shift led to the premature termination of protein translation (Figure 1F). Sequencing peak diagrams showed successful generation of a homozygous *scd* mutant with 13 and 10 bases deleted (Supplementary Figure S2F). We also generated *scdb* knockout zebrafish on a WT background using CRISPR/Cas9. We targeted exon 2 to disrupt the translation of all functional domains (Supplementary Figure S2E). We used genetic screening and sequencing to confirm the mutations and identified two homozygous mutant alleles of *scdb*. Sequencing peak diagrams showed successful generation of a homozygous *scdb* mutant with 19 bases deleted and +5-1 bases inserted (Supplementary Figure S2G). *In situ* hybridization of tissue sections showed that *scd* but not *scdb* was expressed in the ovary and testis. In *scd*-deficient zebrafish, *scd* expression was abolished, and *scdb* was not up-regulated (Figure 1G, H). RT-qPCR analysis showed that the expression of *scd* was significantly down-regulated in $scd^{-/-}$ livers compared with that in WT livers (Figure 1I). In addition, overall growth and appearance of *scdb* mutant zebrafish were similar to WT zebrafish (Supplementary Figure S2H). GC-MS assay further revealed that $scd^{-/-}$ fish showed increased C16:0 and C18:0 content, but significantly decreased C16:1 and C18:1 content (Figure 1J, K). Therefore, we focused on the *scd* mutants in subsequent study.

**Lipid accumulation in abdomen and liver of *scd* mutants**

To better understand the effect of *scd* mutation on zebrafish development, we generated a *CMV:scd* transgenic fish using a bicistronic vector containing a *CMV:scd* expression cassette and *CMV:mCherry* labeling cassette (Figure 2A). In the WT background, *CMV:scd* transgenic overexpression did not alter the phenotype (Supplementary Figure S2H). We crossed the *scd* transgenic zebrafish with the *scd* mutants, then screened the offspring for the *CMV:scd* transgenic *scd* homozygous mutant, $scd^{-/-}$*/Tg(CMV:scd)*, expressing mCherry (Figure 2B). Results showed that the $scd^{-/-}$ mutant adults were significantly shorter and smaller than the WT zebrafish, and this phenotype could be rescued by transgenic overexpression of *scd* in $scd^{-/-}$*/Tg(CMV:scd)* zebrafish (Figure 2C–E), indicating that the observed phenotype was specific to *scd* depletion. No significant differences in the sex ratio were found among the different groups (Figure 2F). The micro-CT results showed obvious fat accumulation in the abdomens of the $scd^{-/-}$ mutants (Figure 2G), as well as a significantly higher fat-to-volume ratio compared to the WT zebrafish (Figure 2H). Therefore, disruption of *scd* in zebrafish significantly retarded body growth and stimulated body fat accumulation, but it did not affect sex differentiation.

As a key enzyme, Scd plays an important role in monounsaturated fatty acid synthesis. Since liver is a key

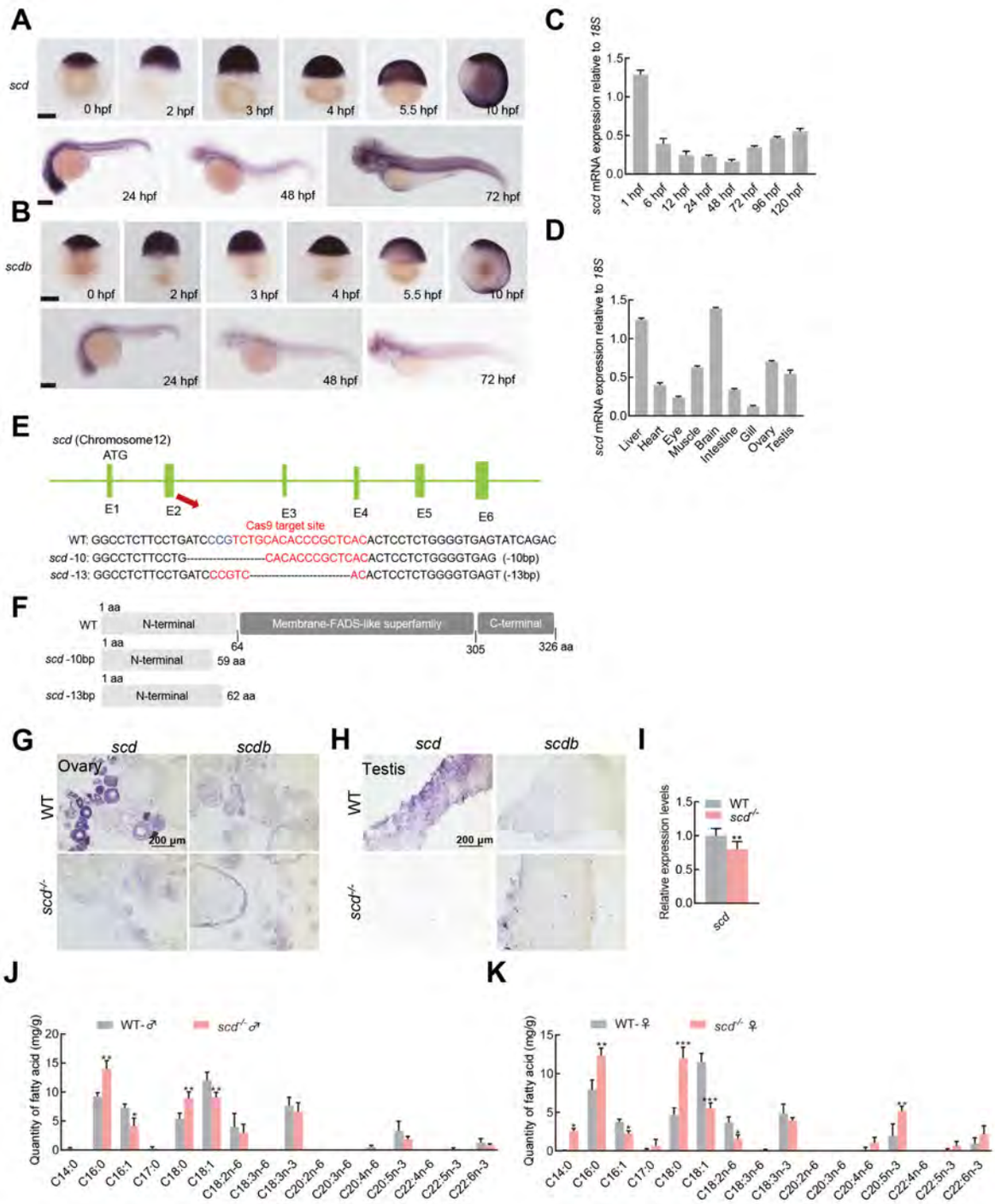


**Figure 1 Generation, identification, and characterization of *scd* mutant**

A: Spatiotemporal expression profiles of *scd* gene detected by embryo *in situ* hybridization. B: Spatiotemporal expression profiles of *scdb* gene detected by embryo *in situ* hybridization. C: RT-qPCR analysis of spatiotemporal expression profile of zebrafish *scd* gene, with *18S* used as a reference gene. D: RT-qPCR analysis of *scd* expression in different adult tissues. E: Schematic of zebrafish *scd* genome locus and gRNA target information. gRNA target sequences are highlighted in red. bp, base pairs; *scd* -13, homozygous mutant line (*scd*$^{-/-}$) with 13 bp (TGCACACCCGCTC) deletion in exon 2 of *scd* gene; *scd* -10, homozygous mutant line with 10 bp (ATCCCGTCTG) deletion in exon 2. F: Predicted WT protein and mutated protein for two mutant alleles. G: Detection of expression patterns of *scd* and *scdb* in ovary by chemical *in situ* hybridization of sections. H: Detection of expression patterns of *scd* and *scdb* in testis by chemical *in situ* hybridization of sections. I: RT-qPCR analysis of *scd* transcriptional expression level in *scd*$^{-/-}$ liver. J: Determination of fatty acid content in WT♂and *scd*$^{-/-}$♂. K: Determination of fatty acid content in WT♀and *scd*$^{-/-}$♀. All values are mean±*SEM*. Student *t*-tests were used. $^{*}$: $P<0.05$; $^{**}$: $P<0.01$; $^{***}$: $P<0.001$.

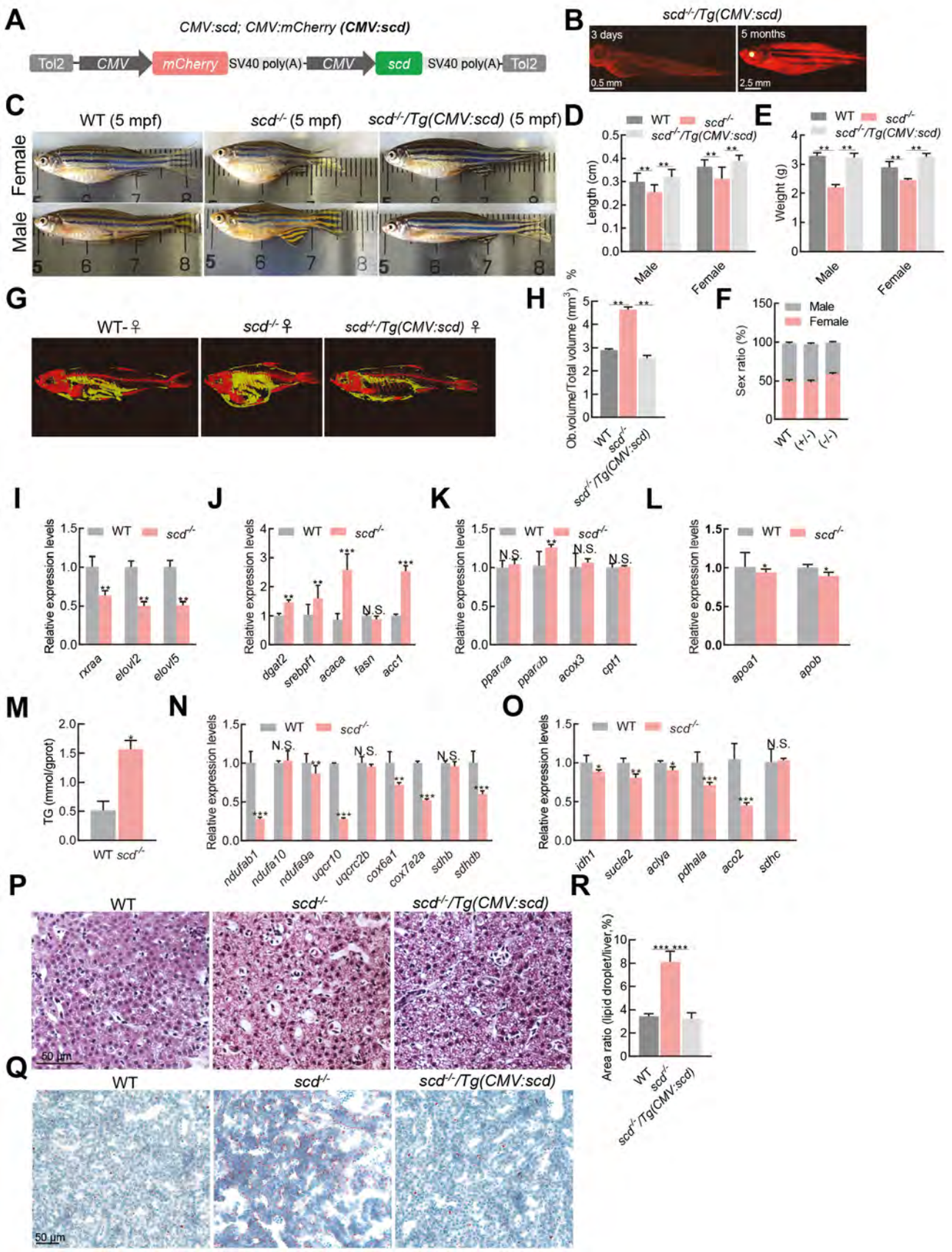
A
CMV:scd; CMV:mCherry (CMV:scd)
Tol2
CMV
mCherry
SV40 poly(A)
CMV
scd
SV40 poly(A)
Tol2
B
scd-/-/Tg(CMV:scd)
3 days
0.5 mm
5 months
2.5 mm
C
WT (5 mpf)
scd-/- (5 mpf)
scd-/-/Tg(CMV:scd) (5 mpf)
Female
Male
D
WT
scd-/-
scd-/-/Tg(CMV:scd)
Length (cm)
Male
Female
E
Weight (g)
F
Male
Female
Sex ratio (%)
WT
(+/-)
(-/-)
G
WT-♀
scd-/-♀
scd-/-/Tg(CMV:scd) ♀
H
Ob.volume/Total volume (mm3) %
WT
scd-/-
scd-/-/Tg(CMV:scd)
I
Relative expression levels
rxraa
elovl2
elovl5
J
dgat2
srebpf1
acaca
fasn
acc1
K
pparαa
pparαb
acox3
cpt1
N.S.
L
apoa1
apob
M
TG (mmol/gprot)
WT
scd-/-
N
ndufab1
ndufa10
ndufa9a
uqcr10
uqcrc2b
cox6a1
cox7a2a
sdhb
sdhdb
O
idh1
sucla2
aclya
pdhala
aco2
sdhc
P
WT
scd-/-
scd-/-/Tg(CMV:scd)
50 μm
Q
WT
scd-/-
scd-/-/Tg(CMV:scd)
50 μm
R
Area ratio (lipid droplet/liver,%)
WT
scd-/-
scd-/-/Tg(CMV:scd)

**Figure 2 Lipid accumulation in the liver of *scd*$^{-/-}$ fish**

A: Schematic of *scd* expression vector *CMV:scd.* B: *scd*$^{-/-}$*/Tg(CMV:scd)* fish at 3 dpf and 5 months old. C: According to morphological analysis, WT females were silver and black, with a round body, while *scd*$^{-/-}$ females were similar in color but had a shorter body and larger abdomen. WT males were orange and black, with a slender body, while *scd*$^{-/-}$ males were similar in color, but shorter in stature with a curved back. D: Body length was significantly shorter in *scd*$^{-/-}$ mutants (*n*=9) than in WT and *CMV-scd* fish (*n*=9) at 6 mpf. E: Bodyweight was significantly lighter in *scd*$^{-/-}$ mutants (*n*=9) than in WT and *CMV-scd* fish (*n*=9) at 6 mpf. F: There was no significant difference in sex ratio between WT fish (*n*=3 groups; no less than 30 in each group) and heterozygous mutants (*n*=3 groups; no less than 30 in each group) or WT fish and homozygous mutants (*n*=3 groups; no less than 30 in each group). G: Micro-CT scan image of WT and *scd*$^{-/-}$ fish. H: Comparison of fat-to-total volume ratio in WT and *scd*$^{-/-}$ fish. I: Expression levels of *rxraa*, *elovl2*, and *elovl5* were significantly down-regulated in *scd*$^{-/-}$ livers compared to WT livers (RT-qPCR analysis) J: Expression levels of fatty acid synthesis-related genes *dgat2*, *srebf1*, *acaca*, *fasn*, and *acc1* were significantly higher in *scd*$^{-/-}$ liver than in WT liver at 3 mpf (RT-qPCR analysis). K: Expression levels of oxidation-related genes *pparαa*, *pparαb*, *acox3*, and *cpt1* in WT and *scd*$^{-/-}$ livers at 3 mpf (RT-qPCR analysis). L: Expression levels of transfer-related genes *apoa1* and *apob* in WT and *scd*$^{-/-}$ livers at 3 mpf (RT-qPCR analysis). M: Triglyceride content in WT and *scd*$^{-/-}$ livers. N: Expression levels of oxidative phosphorylation-related genes *ndufab1*, *ndufa10*, and *ndufa9a* in WT and *scd*$^{-/-}$ livers at 3 mpf (RT-qPCR analysis). O: Expression levels of tricarboxylic acid cycle-related genes *idh1*, *sucla2*, and *aclya* in the WT and *scd*$^{-/-}$ livers at 3 mpf (RT-qPCR analysis). P: H&E staining of liver sections from WT, *scd*$^{-/-}$, and *scd*$^{-/-}$*/Tg(CMV:scd)* fish (*n*=3, two sections for each sample) at 3 mpf. Scale bars, 50 μm. Q: Oil Red staining of liver sections from WT, *scd*$^{-/-}$, and *scd*$^{-/-}$*/Tg(CMV:scd)* fish (*n*=3, two sections for each sample) at 3 mpf. Scale bars, 50 μm. R: Quantitative average area of lipid droplets (*n*=3, two sections for each sample). There were more lipid droplets in *scd*$^{-/-}$ liver than in WT liver. All values are mean±SEM. Student *t*-tests were used. $^{*}$: $P$<0.05; $^{**}$: $P$<0.01; $^{***}$: $P$<0.001; ns: No significance.

metabolic organ, we detected the expression levels of genes related to fatty acid biogenesis in liver samples of fish at 3 months post-fertilization (mpf) by RT-qPCR. Results showed that the liver expression levels of *rxraa*, *elovl2*, and *elovl5* were significantly lower in the *scd*$^{-/-}$ fish than in the controls (Figure 2I). In contrast, the expression level of the sterol regulatory element binding protein-1 gene (*srebf1*), which is involved in the adipogenesis pathway, was significantly higher in the *scd*$^{-/-}$ fish liver than in the control liver (Figure 2J). Two genes involved in fatty acid synthesis (*acc1* and *acaca*) and a key gene related to triglyceride synthesis (*dgat2*) were significantly up-regulated in the liver of *scd*$^{-/-}$ fish (Figure 2J). In addition, the peroxisome proliferation-activated receptor gene *pparαb* was slightly up-regulated in the *scd*$^{-/-}$ fish compared to the WT fish (Figure 2K), suggesting activation of the lipid oxidation pathway in the liver of the *scd*$^{-/-}$ fish. The *cpt1* and *acox3* genes, which are related to liver lipid oxidation, showed no significant differences in the liver of *scd*$^{-/-}$ fish (Figure 2K). Moreover, the *apob* and *apoa1* genes, which are related to very low-density lipoprotein (VLDL) production, were down-regulated in the mutant liver (Figure 2L), indicating that the transfer of triglycerides from the liver as VLDL was inhibited. Subsequently, we found that the *scd*$^{-/-}$ mutants had significantly higher liver levels of triglycerides than the WT fish (Figure 2M). The expression of genes related to oxidative phosphorylation (Figure 2N) and tricarboxylic acid cycle (Figure 2O) were down-regulated in the *scd*$^{-/-}$ liver. We also investigated potential lipid droplet accumulation in the *scd*$^{-/-}$ mutant livers by hematoxylin and eosin (H&E) and Oil Red staining. Compared with the WT fish, the liver cell nucleus of the *scd*$^{-/-}$ fish was small and irregular in shape (Figure 2P). Using Oil Red staining, we found a larger number of lipid droplets in the *scd*$^{-/-}$ livers compared to the WT and *scd*$^{-/-}$*/Tg(CMV:scd)* livers (Figure 2Q, R), suggesting that *scd*$^{-/-}$*/Tg(CMV:scd)* fish may rescue the phenotype of lipid droplet accumulation in *scd*$^{-/-}$ livers.

### Elevated cell apoptosis in *scd* mutant liver

Scanning electron microscopy also showed accumulation of lipid droplets in the *scd*$^{-/-}$ livers (Figure 3A), with shrunken mitochondria in the *scd*$^{-/-}$ mutants (Figure 3B). The opposite results were obtained in *scd*$^{-/-}$*/Tg(CMV:scd)* fish. RT-qPCR analysis showed that the expression levels of *scd*, *rxraa*, *elovl2*, and *elovl5* were significantly up-regulated in *scd*$^{-/-}$*/Tg(CMV:scd)* livers compared to *scd*$^{-/-}$ mutant livers (Figure 3C). The expression levels of *dgat2*, *srebpf1*, *acaca*, *fasn*, *and acc1* were significantly down-regulated in the *scd*$^{-/-}$*/Tg(CMV:scd)* livers compared to the *scd*$^{-/-}$ mutants (Figure 3D). In addition, PPAR genes *pparαa*, *pparαb*, *acox3*, and *cpt1* were down-regulated in *scd*$^{-/-}$*/Tg(CMV:scd)* fish compared to *scd*$^{-/-}$ mutants (Figure 3E). Furthermore, *apoa1* and *apob* were up-regulated in *scd*$^{-/-}$*/Tg(CMV:scd)* fish compared to *scd*$^{-/-}$ mutants (Figure 3F), and the expression levels of genes related to oxidative phosphorylation (Figure 3G) were also up-regulated in the *scd*$^{-/-}$*/Tg(CMV:scd)* livers. These results suggest that transgenic overexpression of *scd* rescues fatty liver in *scd*$^{-/-}$ fish. Previous studies have shown that monounsaturated fatty acids catalyzed by SCD1 can replace polyunsaturated fatty acids in lipid membranes, thereby reducing the accumulation of lipid reactive oxygen species (ROS) and effectively inhibiting ferroptosis (Das, 2019; Magtanong et al, 2019; Tesfay et al, 2019). Ferroptosis is a non-apoptotic form of cell death, characterized by the accumulation of cytotoxic lipid ROS, which leads to fatal lipid membrane damage and perforation (Dixon & Stockwell, 2019; Fang et al, 2019; Gaschler et al, 2018; Hassannia et al, 2019; Murphy, 2018). Research suggests that SCD1 can inhibit ferroptosis and cell apoptosis (Ye et al, 2021). As the *scd*$^{-/-}$ fish exhibited abnormal liver development, we explored whether their livers undergo apoptosis. TUNEL assay confirmed that there were more apoptotic cells in the *scd*$^{-/-}$ livers than in the WT and *scd*$^{-/-}$*/Tg(CMV:scd)* livers (Figure 3H, I), implying that *scd* deficiency in zebrafish accelerates hepatocyte apoptosis.

Apoptosis involves two classic apoptotic pathways, i.e., death receptor activation pathway (exogenous pathway) and mitochondrial damage pathway (endogenous pathway). Caspase-3 plays a vital role in apoptosis induced by various stimulating factors. Here, immunofluorescence indicated that

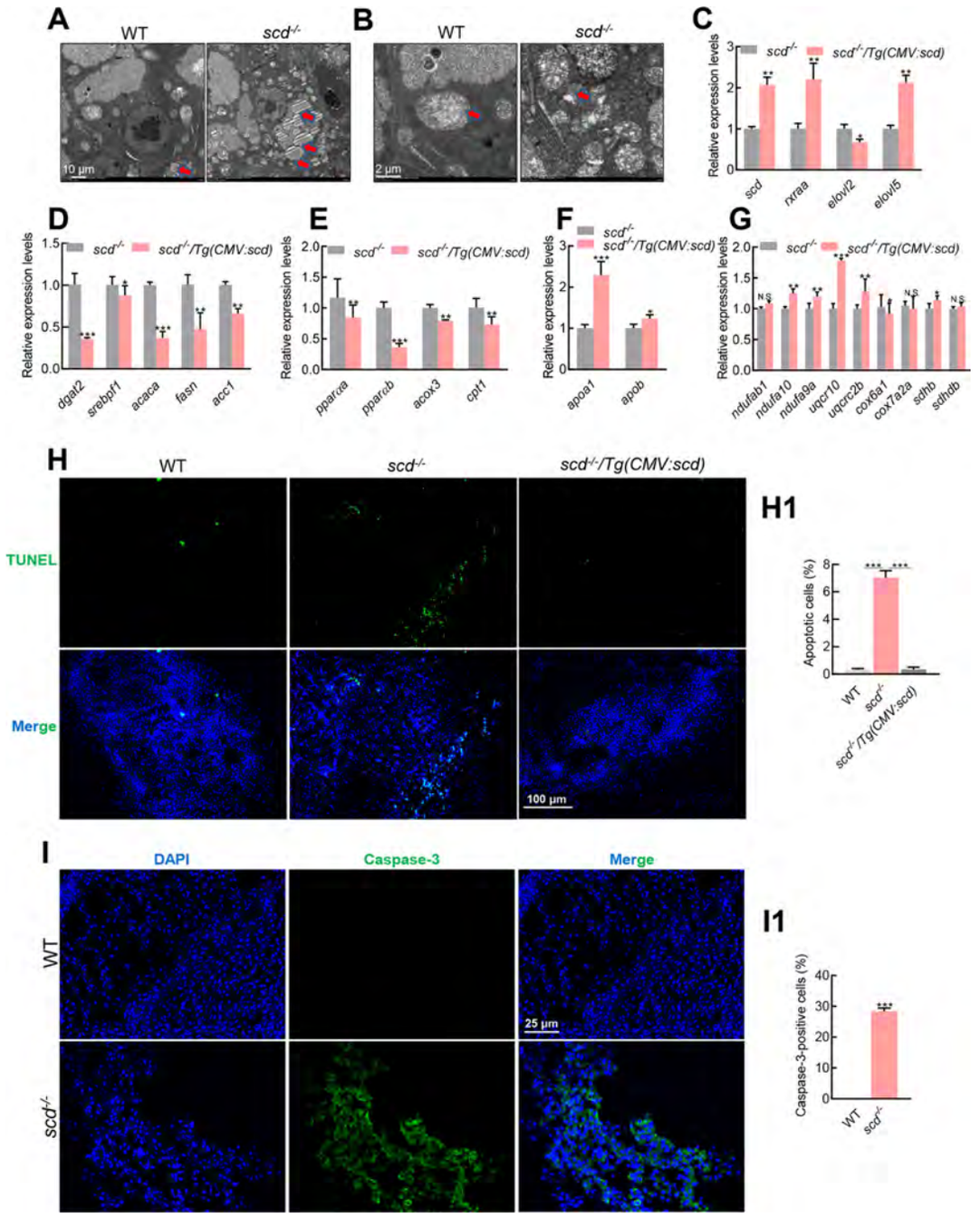


**Figure 3 Lipid accumulation and elevated apoptosis in *scd*$^{-/-}$ livers**

A: Scanning electron micrographs of WT and *scd*$^{-/-}$ liver sections showing increased lipid droplets in mutant livers. Scale bars: 10 μm. B: Scanning electron micrographs of WT and *scd*$^{-/-}$ liver sections showing shrunken mitochondria in mutant liver cells. Scale bars, 2 μm. C: Expression levels of *scd*, *rxraa*, *elovl2*, and *elovl5* in *scd*$^{-/-}$ and *scd*$^{-/-}$*/Tg(CMV:scd)* livers at 3 mpf (RT-qPCR). D: Expression levels of fatty acid synthesis-related genes *dgat2*, *srebf1*, *acaca*, *fasn*, and *acc1* were significantly lower in *scd*$^{-/-}$*/Tg(CMV:scd)* livers than in *scd*$^{-/-}$ livers at 3 mpf (RT-qPCR). E: Expression levels of oxidation-related genes *pparαa*, *pparαb*, *acox3*, and *cpt1* in *scd*$^{-/-}$ and *scd*$^{-/-}$*/Tg(CMV:scd)* livers at 3 mpf (RT-qPCR). F: Expression levels of transfer-related genes *apoa1* and *apob* in *scd*$^{-/-}$ and *scd*$^{-/-}$*/Tg(CMV:scd)* livers at 3 mpf (RT-qPCR). G: Expression levels of oxidative phosphorylation-related genes *ndufab1*, *ndufa10*, and *ndufa9a* in *scd*$^{-/-}$ and *scd*$^{-/-}$*/Tg(CMV:scd)* livers at 3 mpf (RT-qPCR). H: Detection of liver cell apoptosis in WT, *scd*$^{-/-}$, and *scd*$^{-/-}$*/Tg(CMV:scd)* fish (*n*=3, two sections for each sample) at 3 mpf with TUNEL staining, with DAPI blue indicating nucleus and TUNEL green indicating apoptosis signal. Scale bars: 100 μm. H1: Number of apoptotic cells (%) (*n*=3, two sections for each sample). I: Immunofluorescence detection of WT and *scd*$^{-/-}$ liver sections (*n*=3, two sections for each sample) with Caspase-3 antibody. Scale bars: 25 μm. I1: Number of Caspase-3-positive cells (%) (*n*=3, two sections for each sample). All values are mean±*SEM*. Student *t*-tests were used. $^{*}$: $P<0.05$; $^{**}$: $P<0.01$; $^{***}$: $P<0.001$; ns: No significance.

Caspase-3 activation was induced in the *scd*$^{-/-}$ liver, but not in the WT liver (Figure 3J, K), suggesting that apoptosis of the liver cells was caused by Caspase-3 activation.

**RNA-seq analysis of liver tissues of WT and *scd* mutant zebrafish**

RNA-seq analysis was used to explore the cause of fatty liver following *scd* deletion in zebrafish. First, principal component (PCA) cluster analysis indicated that the WT and mutant fish were two independent samples, clustered together separately (Figure 4A). The DEGs are shown in Figure 4B as a volcano plot. Based on pathway enrichment analysis, significantly up-regulated DEGs were enriched in signaling pathways related to sterol, steroid, cholesterol, and lipid biosynthesis (Figure 4C), while significantly down-regulated DEGs were enriched in signaling pathways rated to cellular response to insulin stimulus, acylglycerol metabolism, triglyceride metabolism, and lipid catabolism. Enrichment of these pathways suggests that lipid anabolism was very active, while glyceride and triglyceride metabolism and lipid catabolism processes were hindered.

The genes significantly enriched in the steroid metabolism (Figure 4E), oxidoreductase activity (Figure 4F), carbohydrate derivative (Figure 4G), and glycolipid biosynthesis pathways (Figure 4H) were all up-regulated in the mutant liver compared to the WT liver, whereas genes significantly enriched in the insulin-like growth factor binding (Figure 4I), cellular lipid metabolism (Figure 4J), and mitochondrial membrane pathways (Figure 4K) were all down-regulated compared to WT fish. Therefore, we speculate that the anabolism of lipids, steroids, and cholesterol is accelerated in the liver of zebrafish lacking the *scd* gene, but due to lipid catabolism, glyceride and triglyceride metabolism is slowed down, resulting in increased triglycerides, fatty liver formation, and liver damage, consistent with our results. In addition, we also found down-regulated expression of mitochondrial membrane-related genes. Mitochondria are the main energy source for the body, and mitochondrial damage can lead to insufficient energy, triggering a series of metabolic reactions.

***scd*$^{-/-}$ males show defective mating behavior and smaller genital papillae**

We next examined whether *scd*$^{-/-}$ mutants exhibit abnormal reproduction. In natural mating experiments, we did not succeed in obtaining any embryos when *scd*$^{-/-}$ males were used (Figure 5A, D), suggesting that *scd*$^{-/-}$ males exhibited defective mating behavior. Analysis of mating behavior showed that the contact frequency between the WT pair was significantly higher than that between the *scd*$^{-/-}$ pair or between the WT and *scd*$^{-/-}$ pair (Figure 5B). To determine whether *scd*$^{-/-}$ mutants can produce mature gametes, we performed *in vitro* fertilization assays. Although the fertilization rates of the homozygous mutant gametes were significantly lower than those of the WT gametes, the average fertilization rates of all combinations with *scd*$^{-/-}$ males reached 80% (Figure 5C), suggesting that depletion of *scd* had a mild disturbance on sperm and egg quality. Only two of the four groups achieved natural fertilization (Figure 5D). Successful *scd*$^{-/-}$ embryos were generated via artificial insemination (Figure 5E), suggesting that *scd*$^{-/-}$ mutants can produce functional gametes. Subsequently, we tested the survival rate of *scd*$^{-/-}$ mutants and found that the survival rate of *scd*$^{-/-}$ larvae was only about 30%, significantly lower than that of WT fish (Figure 5F).

We carefully checked the development of secondary sex characteristics, including body size, color, and genital papilla morphology, in *scd*$^{-/-}$ and *scd*$^{-/-}$*/Tg(CMV:scd)* adults (Figure 5G, H). The WT females showed a rounder abdomen and protruding genitals (g1), while *scd*$^{-/-}$ females were shorter and had enlarged abdomens, but similar body color ($n$=6). The WT males were slender, with small genital papillae (h1), orange body color, and orange and black anal fins (h2), while *scd*$^{-/-}$ males had smaller body size and anal fins (h4), and almost invisible genital papillae (h3). In addition, the secondary sex characteristics of *scd*$^{-/-}$*/Tg(CMV:scd)* adults were similar to those of WT adults, both female (g5, g6) and male (h5, h6). Thus, these findings indicate that the *scd* gene is involved in the development of genital papillae in zebrafish.

***scd*$^{-/-}$ males produce mature functional sperm**

We next explored why *scd*$^{-/-}$ males could not achieve natural fertilization. We analyzed the morphological parameters of *scd*$^{-/-}$ gametes and found that *scd*$^{-/-}$ male sperm was comparable in size and shape to WT sperm (Figure 6A). Morphological observations also showed that the ovaries of the mutant females were smaller than those of the WT females (Figure 6C). These data indicate that the *scd*$^{-/-}$ mutants had functionally developed testes and ovaries. The gonadosomatic index (GSI) was significantly higher in *scd*$^{-/-}$ males than in WT males (Figure 6B), and significantly higher in *scd*$^{-/-}$ females than in WT females (Figure 6D). Subsequently, H&E staining of the testes and ovaries revealed that the *scd*$^{-/-}$ mutants produced functional gametes (Figure 6E, F). Immunofluorescence of the testes by Vasa (Figure 6G, G1), Sycp3 (Figure 6H, H1), and Pcna (Figure 6I, I1) antibodies showed similar meiosis and mitosis in the *scd*$^{-/-}$ and WT zebrafish testes at 3 mpf, with differentiated spermatids and many spermatozoa. These results further clarified that the *scd*$^{-/-}$ mutants had a normal gamete production process and functionally mature gametes but were unable to complete natural mating due to abnormal genital papillae.

## DISCUSSION

Although SCD has been widely studied in mammalian models, *scd* has not been functionally characterized in fish. Mice with targeted deletion of the *Scd1* gene are characterized by a lean hypermetabolic phenotype, including resistance to diet-induced and genetically induced obesity, as well as insulin resistance, and significant changes in tremor-free thermogenesis (Dobrzyn et al, 2015; Sampath & Ntambi, 2014). To maintain energy balance, animals use metabolic pathways to adjust and adapt to changes in the external environment. At least two proteins are activated in response to alterations in nutrient availability: i.e., AMPK and $NAD^+$-dependent deacetylase sirtuin-1 (Fulco & Sartorelli, 2008). The AMPK activation system acts as a master switch for glucose and lipid metabolism (Hardie, 2004). AMPK can be

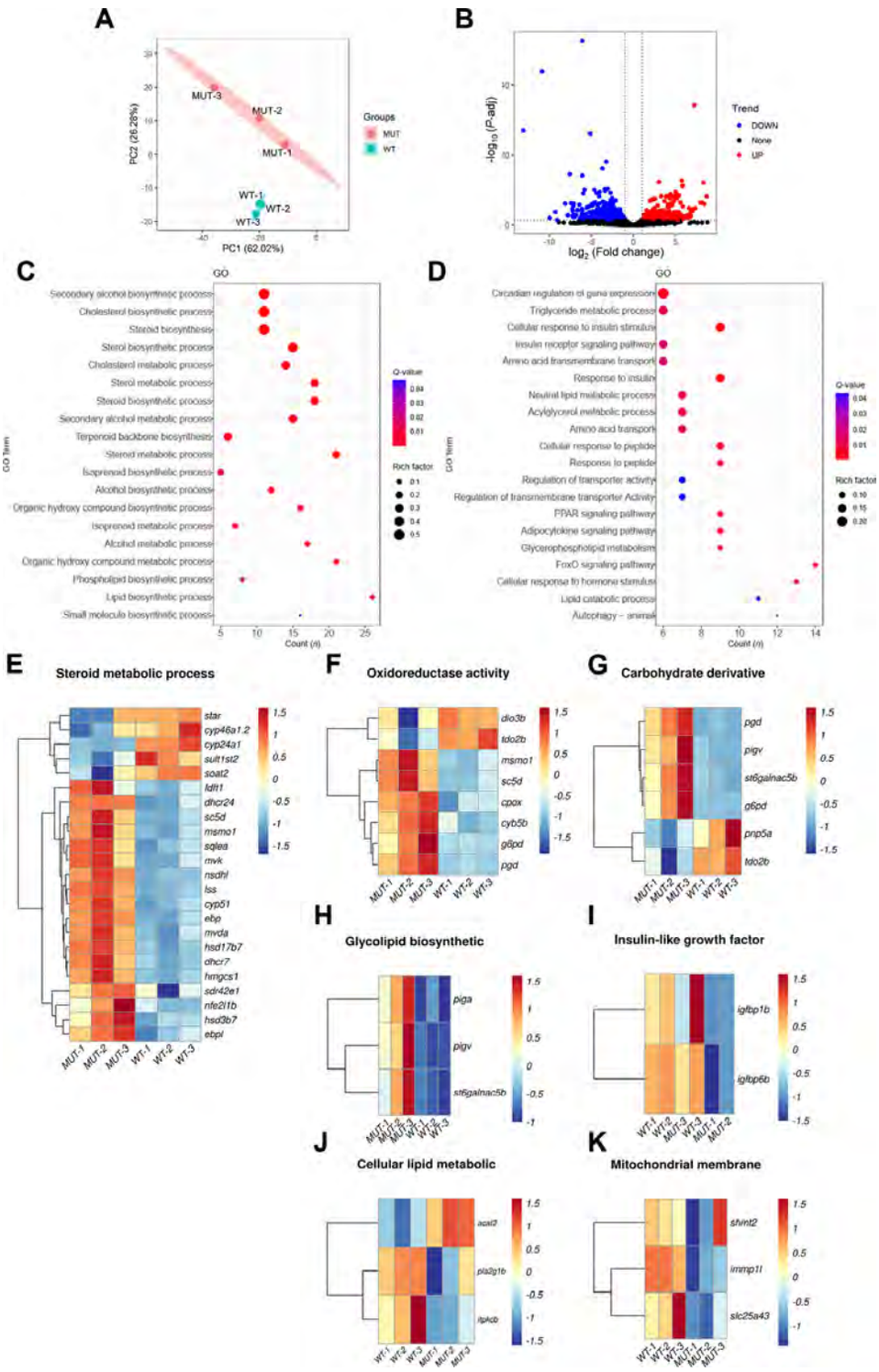


**Figure 4 Analysis of DEGs in WT and *scd*$^{-/-}$ mutant zebrafish liver transcriptomes**

A: PCA cluster analysis of WT and mutant zebrafish liver samples. B: Volcano plot showing DEGs in two sets of samples, where blue represents down-regulated genes, red represents up-regulated genes, black represents genes with no significant difference, and each point represents a gene. C: KEGG analysis of up-regulated DEGs showing significantly enriched pathways D: KEGG analysis of down-regulated DEGs showing significantly enriched pathways. E: Heatmap of DEGs associated with steroid metabolism. F: Heatmap of DEGs associated with oxidoreductase activity. G: Heatmap of DEGs associated with carbohydrate derivative. H: Heatmap of DEGs associated with glycolipid biosynthesis. I: Heatmap of DEGs associated with insulin-like growth factor binding. J: Heatmap of DEGs related to cellular lipid metabolism. K: Heatmap of mitochondrial membrane-associated DEGs.

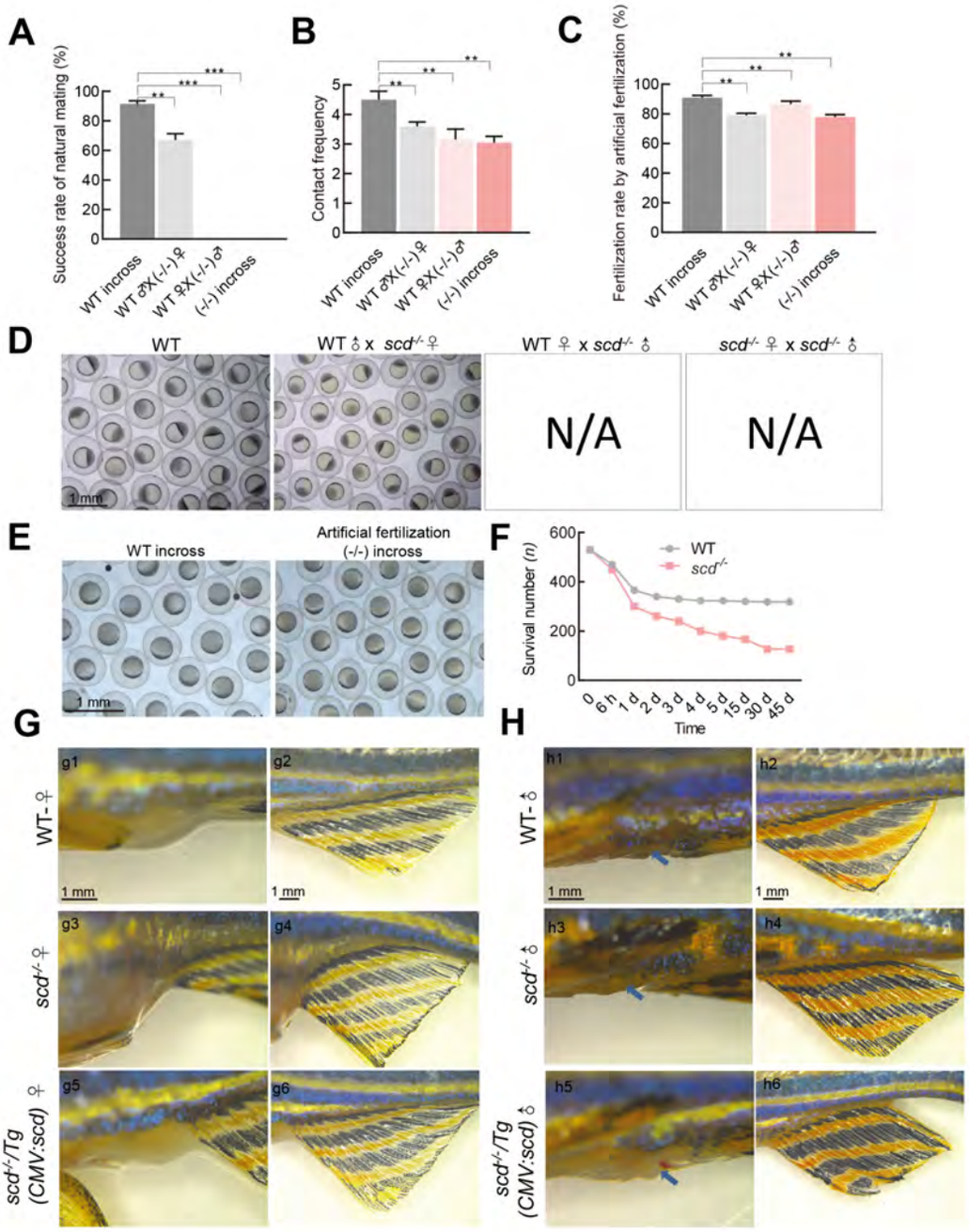


**Figure 5 *scd*$^{-/-}$ males show defective mating behavior and smaller genital papillae**

A: Success rates of natural mating of WT♂×WT♀, WT♂×(-/-)♀, WT♀×(-/-)♂, and (-/-)♂×(-/-)♀ were detected (*n*=10 pairs of fish for each group). B: Contact frequencies between WT♂×WT♀, WT♂×(-/-)♀, WT♀×(-/-)♂, and (-/-)♂×(-/-)♀were detected (*n*=3 pairs of fish for each group). C: Fertilization rate calculated from *in vitro* fertilization using WT sperm+WT egg (WT in-cross), *scd*$^{-/-}$ egg ([-/-]♀)+WT sperm (WT♂), *scd*$^{-/-}$ sperm ([-/-]♂)+WT egg (WT♀), and *scd*$^{-/-}$ sperm ([-/-]♂)+*scd*$^{-/-}$ egg ([-/-]♀) (*n*=3 pair groups were analyzed for each). D: Four natural fertilization groups. E: Representative images from *in vitro* fertilization of *scd*$^{-/-}$ sperm ([-/-]♂)+*scd*$^{-/-}$ egg ([-/-]♀) showing natural fertilized egg development. F: Survival rate of *scd*$^{-/-}$ mutant larvae was ~30%, significantly lower than that of WT larvae. G, H: Morphological analysis of secondary sexual characteristics. WT females had a rounded body shape, silver and black body color, white anal fin (g2), and large extended genital papilla (g1). However, *scd*$^{-/-}$ females had shorter and rounded body shape, silver and black body color, white anal fin (g4), and extended genital papilla (g3). The *scd*$^{-/-}$*/Tg(CMV:scd)* and WT females had the same secondary sexual characteristics (g5, g6). WT males had slim body shape, orange and black body color, orange and black anal fin (h2), and small genital papilla (h1). However, *scd*$^{-/-}$ males had shorter and curved body shape, orange and black body color, orange and black anal fin (h4), and no genital papilla (h3). The *scd*$^{-/-}$*/Tg(CMV:scd)* and WT males had the same secondary sexual characteristics (h5, h6). All values are mean±*SEM*. Student *t*-tests were used. $^{**}$: $P<0.01$; $^{***}$: $P<0.001$. N/A: Not available.

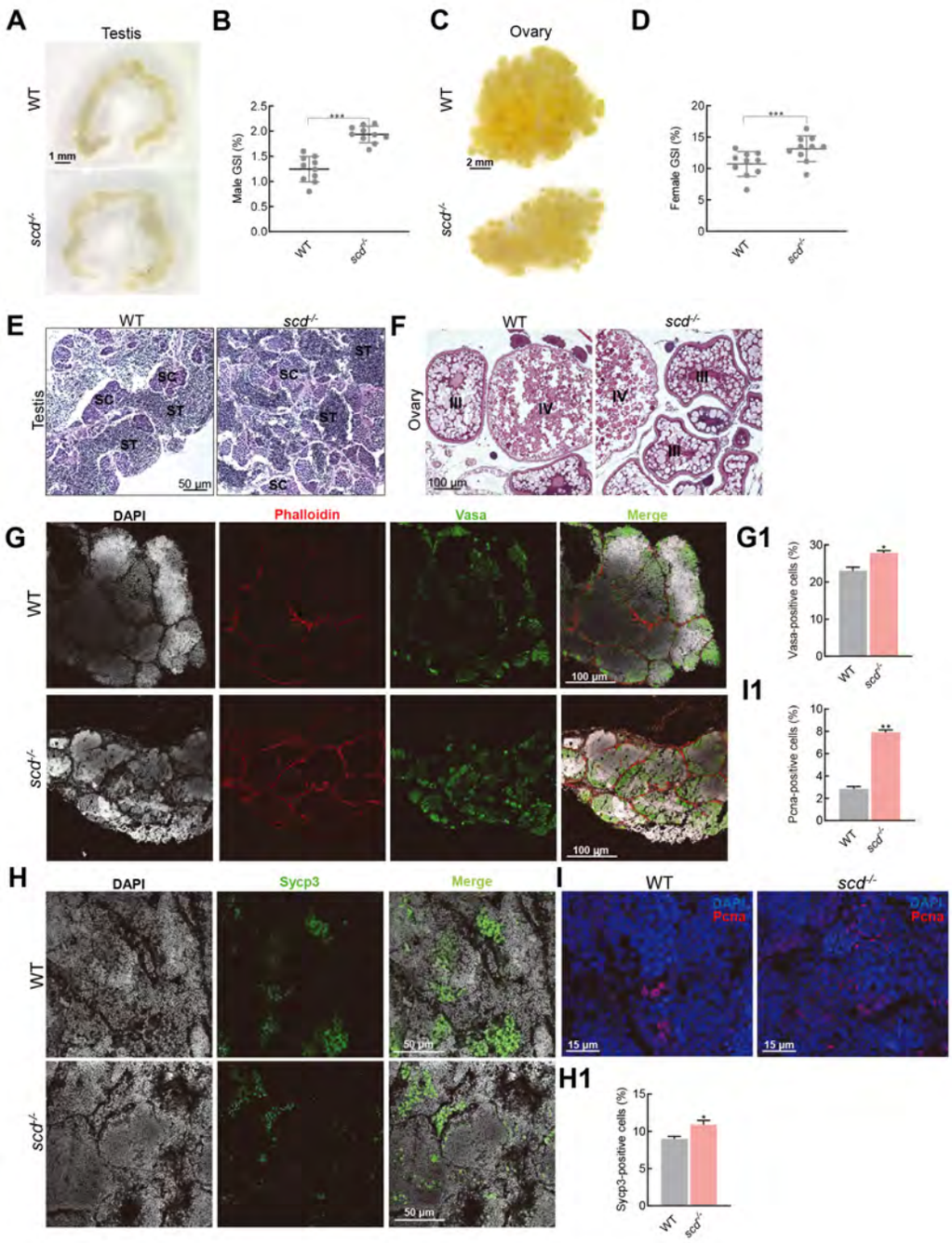


**Figure 6 *scd*$^{-/-}$ males produce functionally mature sperm**

A: Morphological features of *scd*$^{-/-}$ gametes, size and shape of *scd*$^{-/-}$ male testis. Scale bars: 1 mm. B, D: GSI (gonad weight/body weight×100%) of males (B) and females (D) was significantly increased in *scd*$^{-/-}$ mutants compared to WT fish. GSI: Gonadosomatic index. C: Size and shape of *scd*$^{-/-}$ female ovary. Scale bars: 2 mm. E, F: H&E staining of testis (E) and ovary (F) sections from WT and *scd*$^{-/-}$ fish ($n$=3, two sections for each sample) at 3 mpf. Scale bars: 50 μm (E), 100 μm (F). SC, spermatocyte; ST, spermatid. G: Immunofluorescence staining with Vasa antibody of WT and *scd*$^{-/-}$ testes at 3 mpf ($n$=3, three sections for each sample). Scale bars: 100 μm. G1: Quantitative results of average area of Vasa-positive cells ($n$=3, three sections for each sample). There were more germ cells in the *scd*$^{-/-}$ testis than in WT testis. H: Immunofluorescence staining with Sycp3 antibody of WT and *scd*$^{-/-}$ testes at 3 mpf ($n$=3, three sections for each sample). Scale bars: 50 μm. H1: Quantitative results of average area of Sycp3-positive cells ($n$=3, three sections for each sample). There were more meiotic cells in *scd*$^{-/-}$ testis than in WT testis. I: Immunofluorescence staining with Pcna antibody of WT and *scd*$^{-/-}$ testes at 3 mpf ($n$=3, three sections for each sample). Scale bars: 15 μm. I1: Quantitative results of average area of Pcna-positive cells ($n$=3, three sections for each sample). There were more mitotic cells in *scd*$^{-/-}$ testis than in WT testis. All values are mean±*SEM*. Student *t*-tests were used. $^{*}$: $P$<0.05; $^{**}$: $P$<0.01; $^{***}$: $P$<0.001.

phosphorylated by upstream kinases such as LKB1, CaMKKβ, and TAK1, but allosteric regulation of AMPK by AMP appears to be a key component of the overall activation mechanism (Gowans et al, 2013). Changes in lipid metabolism usually lead to changes in skeletal muscle insulin sensitivity (Samuel & Shulman, 2016). Increased SCD activity has been found in people and animals with insulin resistance, and *Scd1* deficiency attenuates diet-induced and genetically induced impaired insulin action (Dobrzyn et al, 2010). However, *Scd1*-disrupted mice exhibit higher glucose tolerance than WT mice due to the down-regulation of protein tyrosine phosphatase 1B and subsequent increase in the activity of insulin receptors and their substrates (Rahman et al, 2003). In this study, we generated a zebrafish *scd* mutant *(scd*$^{-/-}$*)* to elucidate the role of *scd* in lipid metabolism and sexual development and reproduction.

The *scd*$^{-/-}$ fish were characterized by a short stature and enlarged abdomen during development and were significantly shorter than the WT controls at the adult stage. The *scd*$^{-/-}$ fish displayed significantly increased lipid distribution at the whole-body level and a typical fatty liver disease phenotype, which could be rescued by transgenic overexpression of *scd*. The balance between lipogenesis and lipolysis is critical for lipid homeostasis and metabolic health. In this study, lipid droplet accumulation occurred in the liver due to increased fatty acid biosynthesis and lipid storage and decreased fatty acid oxidation and lipolysis (Figure 7). Severe lipid accumulation in the liver led to mitochondrial dysfunction and apoptosis in the hepatocytes. Increasing evidence suggests that the direct anti-stearic effects of SCD1 deficiency stem from increased fatty acid oxidation (Dobrzyn et al, 2005; Dobrzyn et al, 2004; Ntambi et al, 2002). Activation of the AMPK pathway is a key component of this process (Dobrzyn et al, 2005; Dobrzyn et al, 2004). Interestingly, although SCD1 knockout can increase the phosphorylation of AMPK in skeletal muscle, muscle-specific overexpression of SCD1 can lead to a decrease in the phosphorylation level of AMPK and its downstream target acetyl-CoA carboxylase (ACC) in the gastrocnemius muscle. Knockout of the *scd* gene results in diametrically opposite phenotypes in mice and zebrafish, likely due to differences in the way these two types of organisms absorb nutrients. Zebrafish are small vertebrates that do not use carbohydrates efficiently and instead use protein for energy, thus limiting storage of dietary protein. However, as a representative of mammals, mice can utilize both protein and carbohydrates efficiently.

We also found that *scd*$^{-/-}$ males had smaller genital papillae and exhibited defective natural mating but possessed functionally mature gametes. The *scd*$^{-/-}$ females could mate naturally, but the larval survival rate was low. Overall, these findings emphasize that *scd* plays an important role in reproductive development, and that lipid homeostasis is important for sexual development and behavior. In conclusion, our findings reveal that *scd* plays an irreplaceable role in liver lipid metabolism and reproductive development in zebrafish, with depletion of *scd* severely impairing liver metabolism and normal growth and reproduction (Figure 7).

## DATA AVAILABILITY

The genomic and transcriptomic data were submitted to the NCBI GEO database under accession number GSE207660, https://www.ncbi.nlm.nih.gov/geo/query/acc.cgi?acc=GSE207660, GSA database under accession number CRA008031 (https://ngdc.cncb.ac.cn/gsa/), and Science Data Bank under doi:10.57760/sciencedb.j00139.00036. (https://www.scidb.cn/en)

## SUPPLEMENTARY DATA

Supplementary data to this article can be found online.

## COMPETING INTERESTS

The authors declare that they have no competing interests.

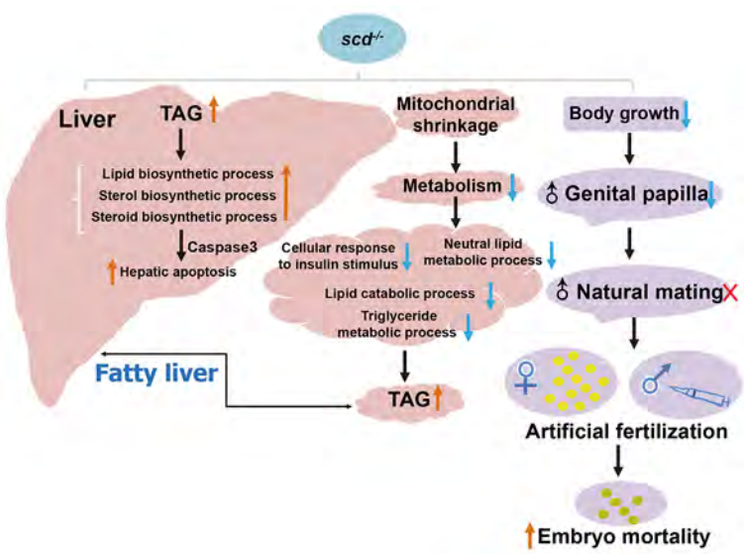


**Figure 7 Graphic summary of *scd* regulation of lipid homeostasis and sexual behavior**

## AUTHORS' CONTRIBUTIONS

Y.H.S. conceived and designed the study. S.Z. and Y.H.S. supervised the analyses. S.S.X., Y.L., H.P.W., and Y.Q.W. prepared the data. W.B.C. performed RNA-seq analysis. S.S.X. and Y.H.S. analyzed the data. S.S.X., Z.W.S., and H.L. prepared the draft of the manuscript. S.S.X. and Y.H.S. revised and finalized the manuscript. All authors read and approved the final version of the manuscript.


## ACKNOWLEDGMENTS

We thank Kuo-Yu Li from the China Zebrafish Resource Center (CZRC) for the many helpful discussions about mutant generation and fish health.


## REFERENCES


Bustin SA, Benes V, Garson JA, Hellemans J, Huggett J, Kubista M, et al. 2009. The MIQE guidelines: minimum information for publication of quantitative real-time PCR experiments. *Clinical chemistry*, **55**(4): 611−622.

Das UN. 2019. Saturated fatty acids, MUFAs and PUFAs regulate ferroptosis. *Cell Chemical Biology*, **26**(3): 309−311.

Dixon SJ, Stockwell BR. 2019. The hallmarks of ferroptosis. *Annual Review of Cancer Biology*, **3**: 35−54.

Dobrzyn A, Dobrzyn P, Lee SH, Miyazaki M, Cohen P, Asilmaz E, et al. 2005. Stearoyl-CoA desaturase-1 deficiency reduces ceramide synthesis by downregulating serine palmitoyltransferase and increasing β-oxidation in skeletal muscle. *American Journal of Physiology–Endocrinology and Metabolism*, **288**(3): E599−E607.

Dobrzyn P, Bednarski T, Dobrzyn A. 2015. Metabolic reprogramming of the heart through stearoyl-CoA desaturase. *Progress in Lipid Research*, **57**: 1−12.

Dobrzyn P, Dobrzyn A, Miyazaki M, Cohen P, Asilmaz E, Hardie DG, et al. 2004. Stearoyl-CoA desaturase 1 deficiency increases fatty acid oxidation by activating AMP-activated protein kinase in liver. *Proceedings of the National Academy of Sciences of the United States of America*, **101**(17): 6409−6414.

Dobrzyn P, Jazurek M, Dobrzyn A. 2010. Stearoyl-CoA desaturase and insulin signaling-What is the molecular switch?. *Biochimica et Biophysica Acta (BBA)–Bioenergetics*, **1797**(6–7): 1189–1194.

Fang XX, Wang H, Han D, Xie EJ, Yang X, Wei JY, et al. 2019. Ferroptosis as a target for protection against cardiomyopathy. *Proceedings of the National Academy of Sciences of the United States of America*, **116**(7): 2672−2680.

Fulco M, Sartorelli V. 2008. Comparing and contrasting the roles of AMPK and SIRT1 in metabolic tissues. *Cell Cycle*, **7**(23): 3669−3679.

Gaschler MM, Andia AA, Liu HR, Csuka JM, Hurlocker B, Vaiana CA, et al. 2018. $FINO_2$ initiates ferroptosis through GPX4 inactivation and iron oxidation. *Nature Chemical Biology*, **14**(5): 507−515.

Gowans GJ, Hawley SA, Ross FA, Hardie DG. 2013. AMP is a true physiological regulator of AMP-activated protein kinase by both allosteric activation and enhancing net phosphorylation. *Cell Metabolism*, **18**(4): 556−566.

Hansen M, Flatt T, Aguilaniu H. 2013. Reproduction, fat metabolism, and life span: what is the connection?. *Cell Metabolism*, **17**(1): 10−19.

Hardie DG. 2004. AMP-activated protein kinase: a master switch in glucose and lipid metabolism. *Reviews in Endocrine and Metabolic Disorders*, **5**(2): 119−125.

Hassannia B, Vandenabeele P, Vanden Berghe T. 2019. Targeting ferroptosis to iron out cancer. *Cancer Cell*, **35**(6): 830−849.

Hölttä-Vuori M, Salo VTV, Nyberg L, Brackmann C, Enejder A, Panula P, et al. 2010. Zebrafish: gaining popularity in lipid research. *Biochemical Journal*, **429**(2): 235−242.

Hulver MW, Berggren JR, Carper MJ, Miyazaki M, Ntambi JM, Hoffman EP, et al. 2005. Elevated stearoyl-CoA desaturase-1 expression in skeletal muscle contributes to abnormal fatty acid partitioning in obese humans. *Cell Metabolism*, **2**(4): 251−261.

Jump DB. 2011. Fatty acid regulation of hepatic lipid metabolism. *Current Opinion in Clinical Nutrition and Metabolic Care*, **14**(2): 115−120.

Kim E, Lee JH, Ntambi JM, Hyun CK. 2011. Inhibition of stearoyl-CoA desaturase1 activates AMPK and exhibits beneficial lipid metabolic effects *in vitro*. *European Journal of Pharmacology*, **672**(1–3): 38–44.

Li LY, Li JM, Ning LJ, Lu DL, Luo Y, Ma Q, et al. 2020. Mitochondrial fatty acid β-oxidation inhibition promotes glucose utilization and protein deposition through energy homeostasis remodeling in fish. *The Journal of Nutrition*, **150**(9): 2322−2335.

Livak KJ, Schmittgen TD. 2001. Analysis of relative gene expression data using real-time quantitative PCR and the $2^{-\Delta\Delta C_T}$2-ddct Method. *Methods*, **25**(4): 402−408.

Magtanong L, Ko PJ, To M, Cao JY, Forcina GC, Tarangelo A, et al. 2019. Exogenous monounsaturated fatty acids promote a ferroptosis-resistant cell state. *Cell Chemical Biology*, **26**(3): 420−432.e9.

Malodobra-Mazur M, Dziewulska A, Kozinski K, Dobrzyn P, Kolczynska K, Janikiewicz J, et al. 2014. Stearoyl-CoA desaturase regulates inflammatory gene expression by changing DNA methylation level in 3T3 adipocytes. *The International Journal of Biochemistry & Cell Biology*, **55**: 40−50.

Miyazaki M, Flowers MT, Sampath H, Chu K, Otzelberger C, Liu XQ, et al. 2007. Hepatic stearoyl-CoA desaturase-1 deficiency protects mice from carbohydrate-induced adiposity and hepatic steatosis. *Cell Metabolism*, **6**(6): 484−496.

Miyazaki M, Jacobson MJ, Man WC, Cohen P, Asilmaz E, Friedman JM, et al. 2003. Identification and characterization of murine SCD4, a novel heart-specific stearoyl-CoA desaturase isoform regulated by leptin and dietary factors. *Journal of Biological Chemistry*, **278**(36): 33904−33911.

Murphy MP. 2018. Metabolic control of ferroptosis in cancer. *Nature Cell Biology*, **20**(10): 1104−1105.

Ntambi JM, Buhrow SA, Kaestner KH, Christy RJ, Sibley E, Kelly TJ, et al. 1988. Differentiation- induced gene expression in 3T3-L1 preadipocytes: characterization of a differentially expressed gene encoding stearoyl-CoA desaturase. *Journal of Biological Chemistry*, **263**(33): 17291−17300.

Ntambi JM, Miyazaki M. 2003. Recent insights into stearoyl-CoA desaturase-1. *Current Opinion in Lipidology*, **14**(3): 255−261.

Ntambi JM, Miyazaki M, Stoehr JP, Lan H, Kendziorski CM, Yandell BS, et al. 2002. Loss of stearoyl-CoA desaturase-1 function protects mice against adiposity. *Proceedings of the National Academy of Sciences of the United States of America*, **99**(17): 11482−11486.

Nyunoya H, Noda T, Kawamoto Y, Hayashi Y, Ishibashi Y, Ito M, et al. 2021. Lack of Δ5 desaturase activity impairs EPA and DHA synthesis in fish cells from Red Sea Bream and Japanese Flounder. *Marine Biotechnology*, **23**(3): 472−481.

Pang SC, Wang HP, Li KY, Zhu ZY, Kang JX, Sun YH. 2014. Double transgenesis of humanized *fat1* and *fat2* genes promotes omega-3 polyunsaturated fatty acids synthesis in a zebrafish model. *Marine Biotechnology*, **16**(5): 580−593.

Quinlivan VH, Farber SA. 2017. Lipid uptake, metabolism, and transport in the larval zebrafish. *Frontiers in Endocrinology*, **8**: 319.

Rahman SM, Dobrzyn A, Dobrzyn P, Lee SH, Miyazaki M, Ntambi JM. 2003. Stearoyl-CoA desaturase 1 deficiency elevates insulin-signaling components and down-regulates protein-tyrosine phosphatase 1B in muscle. *Proceedings of the National Academy of Sciences of the United States of America*, **100**(19): 11110−11115.

Sampath H, Ntambi JM. 2014. Role of stearoyl-CoA desaturase-1 in skin integrity and whole body energy balance. *Journal of Biological Chemistry*, **289**(5): 2482−2488.

Samuel VT, Shulman GI. 2016. The pathogenesis of insulin resistance: integrating signaling pathways and substrate flux. *The Journal of Clinical Investigation*, **126**(1): 12−22.

Sun SX, Castro F, Monroig Ó, Cao XJ, Gao J. 2020a. *fat-1* transgenic zebrafish are protected from abnormal lipid deposition induced by high-vegetable oil feeding. *Applied Microbiology and Biotechnology*, **104**(17): 7355−7365.

Sun YH, Zhang B, Luo LF, Shi DL, Wang H, Cui ZB, et al. 2020b. Systematic genome editing of the genes on zebrafish Chromosome 1 by CRISPR/Cas9. *Genome Research*, **30**(1): 118−126.

Tabor DE, Xia YR, Mehrabian M, Edwards PA, Lusis AJ. 1998. A cluster of stearoyl CoA desaturase genes, *Scd1* and *Scd2*, on mouse Chromosome 19. *Mammalian Genome*, **9**(4): 341−342.

Tesfay L, Paul BT, Konstorum A, Deng ZY, Cox AO, Lee J, et al. 2019. Stearoyl-CoA desaturase 1 protects ovarian cancer cells from ferroptotic cell death. *Cancer Research*, **79**(20): 5355−5366.

Thisse C, Thisse B. 2008. High-resolution *in situ* hybridization to whole-mount zebrafish embryos. *Nature Protocols*, **3**(1): 59−69.

Van Elswyk ME. 1997. Comparison of *n*-3 fatty acid sources in laying hen rations for improvement of whole egg nutritional quality: a review. *British Journal of Nutrition*, **78**(1): S61−S69.

Wang YQ, Ye D, Zhang FH, Zhang R, Zhu JW, Wang HP, et al. 2022. *Cyp11a2* is essential for oocyte development and spermatogonial stem cell differentiation in zebrafish. *Endocrinology*, **163**(2): bqab258.

Ye D, Tu YX, Wang HP, He MD, Wang YQ, Chen ZF, et al. 2022. A landscape of differentiated biological processes involved in the initiation of sex differentiation in zebrafish. *Water Biology and Security*, **1**(3): 100059.

Ye Z, Zhuo QF, Hu QS, Xu XW, Liu MQ, Zhang Z, et al. 2021. FBW7-NRA41-SCD1 axis synchronously regulates apoptosis and ferroptosis in pancreatic cancer cells. *Redox biology*, **38**: 101807.

Zhang QF, Ye D, Wang HP, Wang YQ, Hu W, Sun YH. 2020. Zebrafish *cyp11c1* knockout reveals the roles of 11-ketotestosterone and cortisol in sexual development and reproduction. *Endocrinology*, **161**(6): bqaa048.

Zhang XF, Pang SC, Liu CJ, Wang HP, Ye D, Zhu ZY, et al. 2019. A novel dietary source of EPA and DHA: metabolic engineering of an important freshwater species-common carp by *fat1*-transgenesis. *Marine Biotechnology*, **21**(2): 171−185.

Zheng Y, Prouty SM, Harmon A, Sundberg JP, Stenn KS, Parimoo S. 2001. *Scd3*-A novel gene of the stearoyl-CoA desaturase family with restricted expression in skin. *Genomics*, **71**(2): 182−191.

Zou Y, Wang YN, Ma H, He ZH, Tang Y, Guo L, et al. 2020. SCD1 promotes lipid mobilization in subcutaneous white adipose tissue. *Journal of Lipid Research*, **61**(12): 1589−1604.